Uniform luminescent carbon nanodots prepared by rapid pyrolysis of organic precursors confined within nanoporous templating structures

M.C. Ortega-Liebana [a, b, 1], N.X. Chung [c, 1], R. Limpens [c], L. Gomez [c, *], J.L. Hueso [a, b, **], J. Santamaria [a, b], T. Gregorkiewicz [c]

[a] Institute of Nanoscience of Aragon (INA) and Department of Chemical Engineering and Environmental Technology, Edificio I+D+i, Campus Rio Ebro, 50018, Zaragoza, Spain
[b] Networking Research Center on Bioengineering, Biomaterials and Nanomedicine (CIBER-BBN), 28029, Madrid, Spain
[c] Institute of Physics, University of Amsterdam, Science Park 904, 1098 XH, Amsterdam, The Netherlands

ARTICLE INFO

ABSTRACT

Although several methods on the preparation of carbon nanodots (CNDs) emitting throughout the visible have been recently reported, in most of the processes the product suffers from inhomogeneity in size and shape limiting their impact. Here, we report the synthesis of undoped and nitrogen-doped luminescent carbon nanodots by rapid pyrolysis using ordered mesoporous silica nanorods as confining templates. A rapid thermal decomposition (pyrolysis) within the confined dimensions of their pores leads to a highly uniform size distribution of CNDs with average sizes below 4 nm. These CNDs are synthesized in an extremely short time period (5 min of reaction) by immersion in a fluidized-bed reactor that provides heating homogeneity and ensures fast heat transfer. In addition, a rapid release of the homogeneous CNDs can be easily achieved by a simple ultrasonication-filtration step that prevents further chemical action on the mesoporous templates. The emission of both undoped and N-doped CNDs in colloidal and solid state (with an efficiency of 1—5%) originates from a combination of quantum confinement effects and the presence of oxidized surface states; N-doping introduces resonant absorption states which participate in emission. Furthermore, we present a simple model to describe the excitation-dependent/-independent mechanism of carbon nanodots.

1. Introduction

Carbon nanomaterials (graphene, fullerenes, nanotubes, and carbon nanodots (CNDs) in particular) have been widely studied during the past years due to their optoelectronic properties and their potential applications [1]. The most exciting property of CNDs is their photoluminescence (PL), which can be tuned by varying the excitation wavelength [2,3]. Furthermore, they show low toxicity and can be synthesized from an unlimited number of carbon sources, with feasible large scale production and excellent chemical- and photo-stability [4—6]. CNDs have been successfully used for different purposes, such as sensing, bio-imaging, drug delivery, photocatalysis, and photovoltaics [7—10].

The PL mechanism of CNDs and its excitation dependence have been studied in-depth and related to numerous effects, such as quantum confinement (QCE), surface traps and solvent polarity (or "giant red-edge effect"). However, a clear and unified theory is still missing [11]. One of the issues is the CNDs' variability as their composition, structure and properties depend on the raw materials used as carbon sources and the production method (temperature, pressure, solvent) employed.

Numerous synthetic routes have been reported for the production of CNDs, such as laser ablation [12], electrochemical oxidation [13], electrochemical etching [14—16], microwave assisted reaction [17] and hydrothermal synthesis [18]. Nonetheless, the control of the process to yield a product homogeneous in size and shape is still challenging. Also, clean and efficient methods to reduce processing times are needed. A possible approach to obtain a uniform material is to use an external template able to restrict the

* Corresponding author. Institute of Physics, University of Amsterdam, Science Park 904, 1098 XH, Amsterdam, The Netherlands.
** Corresponding author. Institute of Nanoscience of Aragon (INA) and Department of Chemical Engineering and Environmental Technology, Edificio I+D+i, Campus Rio Ebro, 50018, Zaragoza, Spain.
E-mail addresses: L.gomeznavascues@uva.nl (L. Gomez), jlhueso@unizar.es (J.L. Hueso).
[1] Equal contribution.

size and shape of the generated nanostructures. In this regard, micelles [19], mesoporous silica [20] and zeolites [21] have already been used as confining nanoreactors in the production of CNDs. On the other hand, the production of CNDs by pyrolysis (thermal decomposition at high temperatures in the absence of oxygen) is revealed as a simple and efficient method [22]. Therefore, an ideal methodology to synthesize CNDs would be to place the carbon precursor within the pores of an inorganic structure able to withstand the conditions required for pyrolysis. Baldovi et al. [21] proposed this idea using zeolites. However, this required long reaction times of up to 24 h and restricted pore sizes to the sub-nanometric range that involved additional chemical or purification steps to retrieve the CNDs.

Here, we report the synthesis of undoped and N-doped CNDs obtained by a rapid pyrolysis method using ordered mesoporous silica nanorods as hosting nanotemplates. These silica-based nanostructures have been successfully used to: (i) load two different organic precursors such as citric acid (CA) or ethylenediaminetetraacetic acid (EDTA), (ii) induce their thermal decomposition (pyrolysis) within the confined dimensions of their porous walls, and (iii) render a highly uniform size distribution of CNDs. This work attempts to shed light on the PL behavior of CNDs without incurring into the necessity of dissolving the mesoporous silica structure. In many of the common CNDs synthesis methods, a variety of shapes and compositions are possible, due to: (i) the gradients of temperature and concentration that inevitably appear in the batch processes leading to different growth rates for different regions of the reactor and (ii) the possibility of agglomeration of growing nanoparticles during the long synthesis processes. By confining the precursors into a porous structure we expect to alleviate both problems. Also, by accelerating the synthesis process, the opportunity for agglomeration would also be minimized. In addition, the rapid pyrolysis method used allows the syntheses to be completed in a short period of time (5 min of reaction) by immersion in a fluidized-bed reactor that provides a fast heating and a high homogeneity in the heating environment [23,24]. The structure of the silica hosting matrix allowed the synthesis of undoped and N-doped CNDs simply by changing the nature of the precursor hosted in the pores. On the other hand, the high aspect ratio of the nanorods provides a longer diffusion path favoring a high degree of pyrolysis within the pores. Furthermore, the CNDs were successfully retrieved from the mesoporous template by simple ultrasonication and in the absence of additional chemical treatments involving the digestion of the template. The influence of the incorporation of dopants such as nitrogen, which is known to alter the optoelectronic characteristics of CNDs [25,26], has been evaluated by a thorough analysis of the chemical and optical properties of both products, undoped and N-doped CNDs.

2. Experimental

2.1. Chemicals

Tetraethylorthosilicate (TEOS, 98%), hydrochloric acid (HCl, 37%), ammonium fluoride (NH$_4$F, 98%), heptane (99%), poly(-ethylene glycol)-block-poly(propylene glycol)-block-poly(ethylene glycol) average M$_n$ ~5800 (Pluronic$^®$ P-123), lithium chloride anhydrous (LiCl, 99%), sodium chloride (NaCl, 99%), potassium nitrate (KNO$_3$, 99%), citric acid (CA, 99.5%) and ethylenediaminetetraacetic acid (EDTA, 99.995%) were obtained from Sigma-Aldrich. All chemicals were of analytical purity grade.

2.2. Synthesis of ordered mesoporous silica nanorods

Ordered mesoporous silica nanorods were prepared by a slightly modified hydrothermal synthesis according to previously reported procedure [27]. In a typical synthesis, 1.2 g of P-123 and 0.014 g of NH$_4$F were first dissolved at 20 °C in 40 mL of HCl (1.75 M) solution under stirring. Upon complete dissolution, 2.75 mL of TEOS and 8.5 mL of heptane were added drop wise and left under stirring for 8 min. The aged precursor mixture was hydrothermally heated at 100 °C for 24 h in a Teflon-lined autoclave. The solid product was then filtered, washed three times with distilled water, and dried at 60 °C overnight. The removal of the organic template was carried out by calcination with a heating ramp of 1 °C min^{-1} up to 550 °C and a dwell time of 6 h in flowing air.

2.3. Synthesis of undoped and N-doped carbon nanodots

In a typical experiment, 200 mg of the calcined silica nanorods and 100 mg of the selected organic precursor (citric acid or EDTA) were mixed and sonicated in 0.5 mL of a solution containing NaCl, LiCl and KNO$_3$ (mass ratio 20:5:5). The mixture was dried in an oven at 60 °C for 10 min and a fraction of the resulting powder (20 mg) was placed in a quartz capillary (Ø$_{in}$ = 8 mm) designed with inlet-outlet outfits (Ø$_{in}$ = 6 mm) for inert gas feeding (nitrogen flow rate 3 L h^{-1}). The capillary tube was introduced inside a sand fluidized bed (8 cm bed height) used to induce the formation of a bubbling fluidized bed via air bubbling (flow feeding rate 15 L h^{-1}) (see Fig. 1). This fluidized bed configuration promotes a rapid and homogeneous heating during the rapid pyrolysis process carried out by immersion of the tubular reactor containing the mesoporous solids inside the bubbling fluidized bed set at 500 °C under the inert atmosphere provided by nitrogen. The fluidized bed was kept at 500 °C for 5 min and allowed to cool down to room temperature. After the flash pyrolysis process, a brownish-pale yellow solid was obtained. This powdered solid was extensively rinsed and ultrasonicated in water for 15 min to facilitate the release of the carbon nanostructures generated within the silica nanoreactor. The supernatant containing the CNDs was passed through a 10 nm cutoff filter. The final yellow solution containing the CNDs was stored without any further treatment prior to use. The experiments have been performed by the platform of Production of Biomaterials and Nanoparticles of the NANBIOSIS ICTS, more specifically by the Nanoparticle Synthesis Unit of the CIBER in BioEngineering, Biomaterials & Nanomedicine (CIBER-BBN).

2.4. Characterization techniques

The morphologies and particle size distributions were determined by transmission electron microscopy (TEM) (FEI Tecnai T20 and Titan^3 High-Base operated at 200 kV and 300 kV, respectively). To prepare the samples, the nanoparticle suspensions were diluted with water prior drop-casting on a holey copper grid. The average size distribution of CNDs was statistically estimated over 200 particle counts. The surface chemistry analysis of the nanoparticles was carried out by Fourier transform infrared (FTIR) spectroscopy using a Bruker Vertex 70 FTIR spectrometer using the horizontal attenuated total reflectance (ATR) mode and by X-ray photoelectron spectroscopy (XPS) with an Axis Ultra DLD (Kratos Tech.). A monochromatic Al Kα source (1486.6 eV) was employed with multiple runs at 12 kV, 10 mA and pass energy of 20 eV. The binding energies were calibrated to the internal C1s (284.2 eV) standard. Curve-fittings were performed with CasaXPS software, using a weighted sum of Lorentzian and Gaussian components after Shirley background subtraction. Raman spectra were acquired with a Laser Raman WiTec Alpha 300 spectrometer using the green exciting radiation (532 nm) from an Ar$^+$ ion laser. All measurements were performed at room temperature.

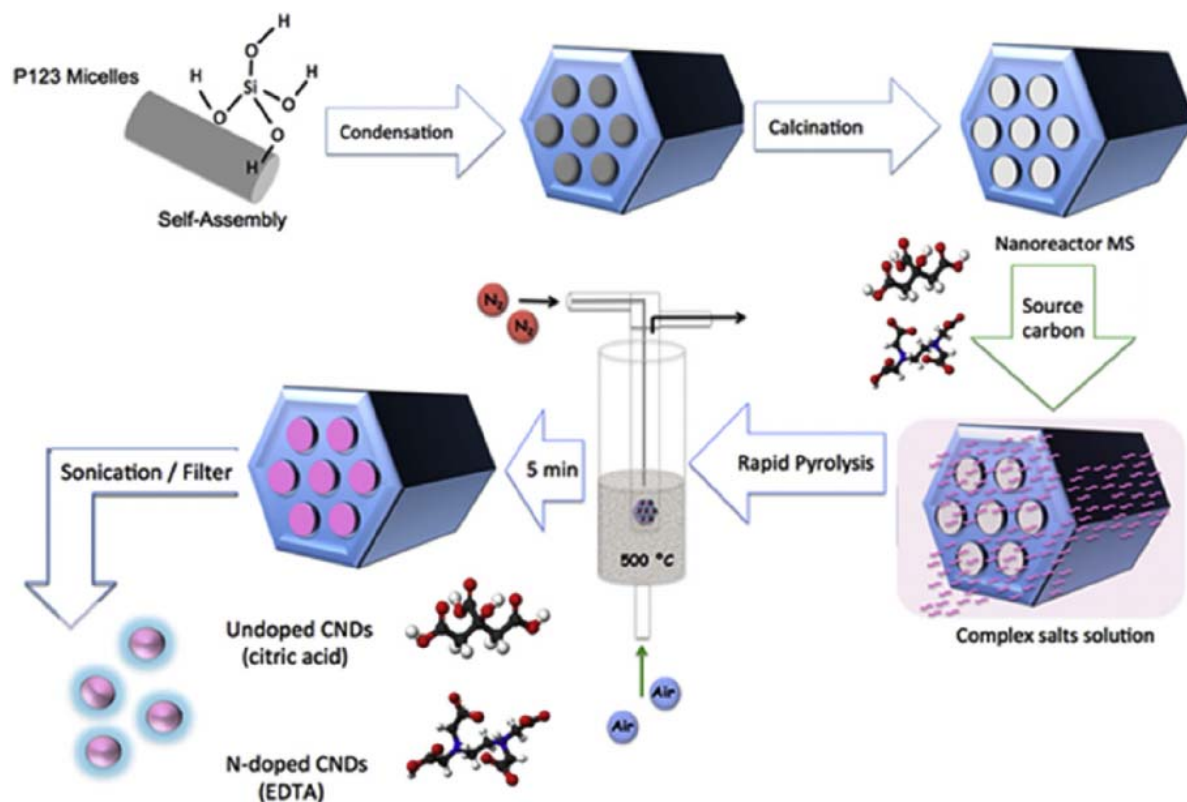The PLE spectra of concentrated undoped and N-doped CNDs

Fig. 1. Scheme describing the different steps carried out to synthesize the mesoporous silica nanorod templates, the nanochannels loading with either citric acid or EDTA, and the rapid pyrolysis treatment carried out in the fluidized bed reactor at 500 °C to render confined undoped and N-doped CNDs, respectively. (A colour version of this figure can be viewed online.)

samples were measured using a Horiba Fluorolog-21 spectrofluorometer with a xenon lamp as an excitation source. Absorption measurements of these samples were conducted with a Perkin Elmer UV–Vis Lambda 950 spectrometer. To prevent absorption saturation in the high absorption regime, we diluted the above undoped and N-doped colloidal samples 15 and 10 times, respectively. The absolute photoluminescence quantum yield (PL QY) measurements were performed in a Newport integrating sphere in order to avoid problems dealing with directionality of reflectance, scattering and emission from these samples; a xenon lamp coupled to a Solar MSA130 monochromator was used to reach a stable and low excitation intensity regime. We used the 7.5 cm and 10 cm integrating spheres to measure PL QY of solid state and colloidal samples, respectively. The details can be found in the Supporting Information.

The nanosecond PL dynamics were measured by using the frequency-doubled output of a tunable Ti:sapphire laser system (Chameleon Ultra, Coherent) providing 140 fs pulses at $\lambda_{exc} = 360$ nm with the repetition frequency of 8 MHz, and the PL emission was detected using a Newport CS260-02 monochromator coupled to a MCP Hamamatsu detector Hamamatsu (R3809U-51).

The PL dynamics were investigated at 430, 445 and 460 nm. For each of them, 2 different excitation powers were employed to validate the linear excitation regime in terms of the relevant parallel PL dynamic traces (in logarithmic scale), as can be seen in Fig. S1. To calculate the lifetime from the dynamics traces, we divide the time window into 2 parts:

(1) For relatively long delay times (multiple nanoseconds), the decay dynamics trace follows a single exponential decay:

$$I_{PL}^{part1} = I_0 \exp\left(-\frac{t}{\tau_{single}} \right) + I_{BGN}$$

With I_0 the initial amplitude, t the delay time, I_{BGN} the background signal and τ_{single} is the single exponential lifetime.

(2) For short time delays, directly after the pulse, the PL mechanism is fitted in terms of the sum of a stretch exponential and the before mentioned single exponential function:

$$I_{PL}^{part2} = I_0 \exp\left(-\frac{t}{\tau_{single}} \right) + I_1 \exp\left[-\left(\frac{t}{\tau_{stretch}} \right)^{\beta} \right] + I_{BGN}$$

With I_1 is the amplitude of the stretch exponential function, β the stretching exponent and $\tau_{stretch}$ the lifetime of the stretched function.

3. Results and discussion

3.1. Rapid pyrolysis of organic precursors hosted within rod-shaped mesoporous silica templates and morpho-chemical characterization of undoped and N-doped CNDs

Fig. 1 shows a scheme of the different synthesis steps carried out to obtain the CNDs. SBA-15 rod-shaped silica mesostructures with straight parallel porous channels were synthesized in first place following a hydrothermal approach previously reported by Oden et al. where reaction times were shortened to ensure the formation of rods in the nanoscale [27] (see Fig. 2a and b for SEM and TEM
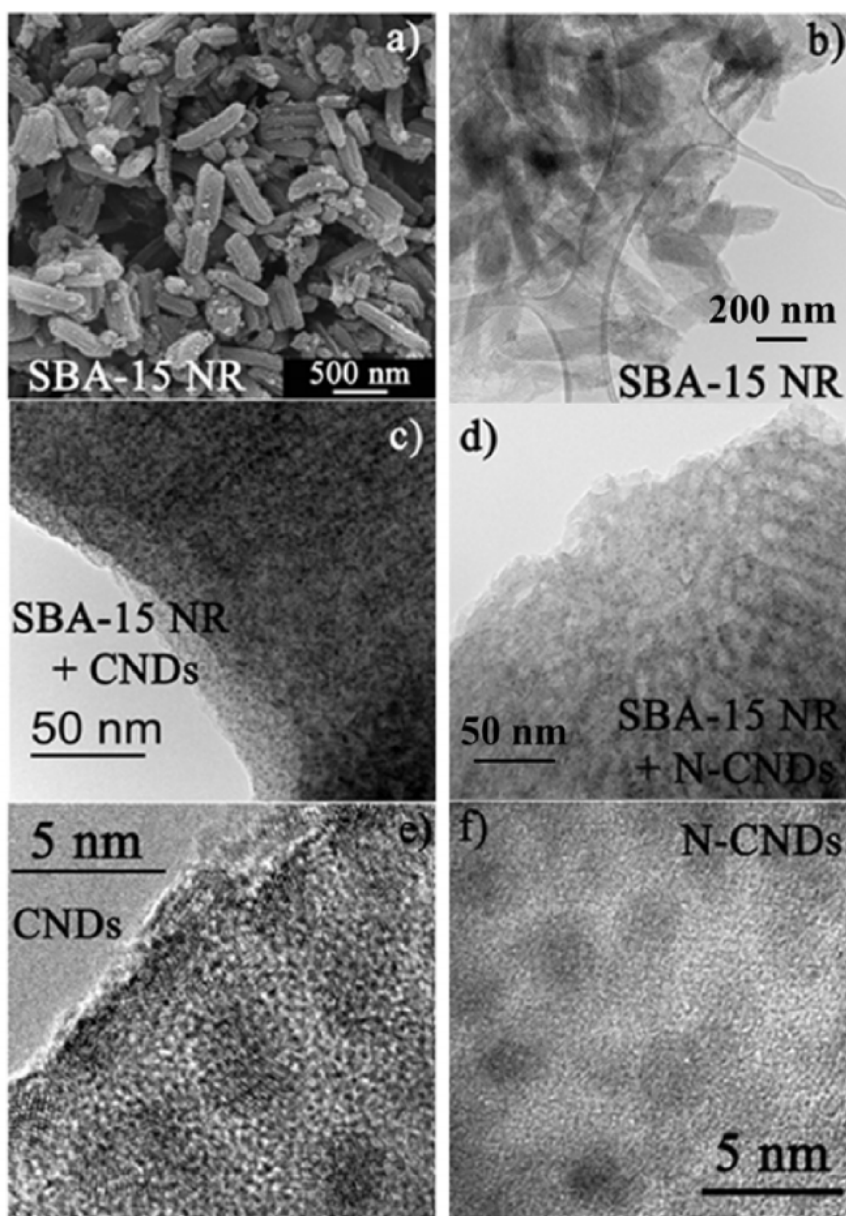
Fig. 2. (a) SEM and (b) TEM images of SBA-15 nanorods after calcination without carbon precursor. (c, d) TEM images showing the loading and confining of CNDs within the mesochannels of SBA-15 nanorods after the flash pyrolysis treatment of CA and EDTA in the fluidized-bed reactor, respectively. (e, f) High-resolution TEM detail of the CNDs encased within the mesoporous SBA-15 nanorods.

images of the SBA-15 nanorods, respectively). Calcination was required to remove the P-123 surfactant used as structuring agent and release the pores. After calcination, the SBA-15 nanorods were immersed in a suspension containing different salts (see Experimental Section) and the organic precursors to be loaded within the channels of the porous support (either citric acid or EDTA containing amine groups to promote N-doping). Subsequently, the loaded SBA-15 pellets were subjected to rapid pyrolysis treatment by immersion within a bubbling fluidized sand bed at 500 °C in the presence of an inert atmosphere of nitrogen. Thermogravimetric analysis revealed that an effective loading of the organic precursors was successfully achieved (up to 33% wt. loading that diminished to approximately 25% wt. after the pyrolysis treatment).

This reactor configuration enabled the effective pyrolysis of the

organic precursors selected as carbon sources and the formation of multiple CNDsencased within the channels of the silica nanoreactor after only 5 min of reaction, as shown in Fig. 2c and d. High-resolution TEM analysis of the freestanding CNDs further corroborates their crystalline structure (Figs. 2e, f and 3c, d). Lattice spacings of 0.210 nm and 0.180 nm corresponding to (100) and (102) diffraction planes of graphite have been identified in Fig. 3c. Likewise, the N-doped CNDs also exhibited a similar crystallinity in spite of their lower mean sizes and 0.204 nm spacings of the (101) diffraction planes in graphite have been also identified in selected nanoparticles (Fig. 3d). In addition, Fig. 3a and b and S4 show the extremely good self-assembly layers of the freestanding CNDs successfully retrieved from the rod-shaped SBA-15 nanotemplates after rinsing, ultrasonication and filtration steps (see Fig. 1 and Experimental Section). This is attributable to the narrow size
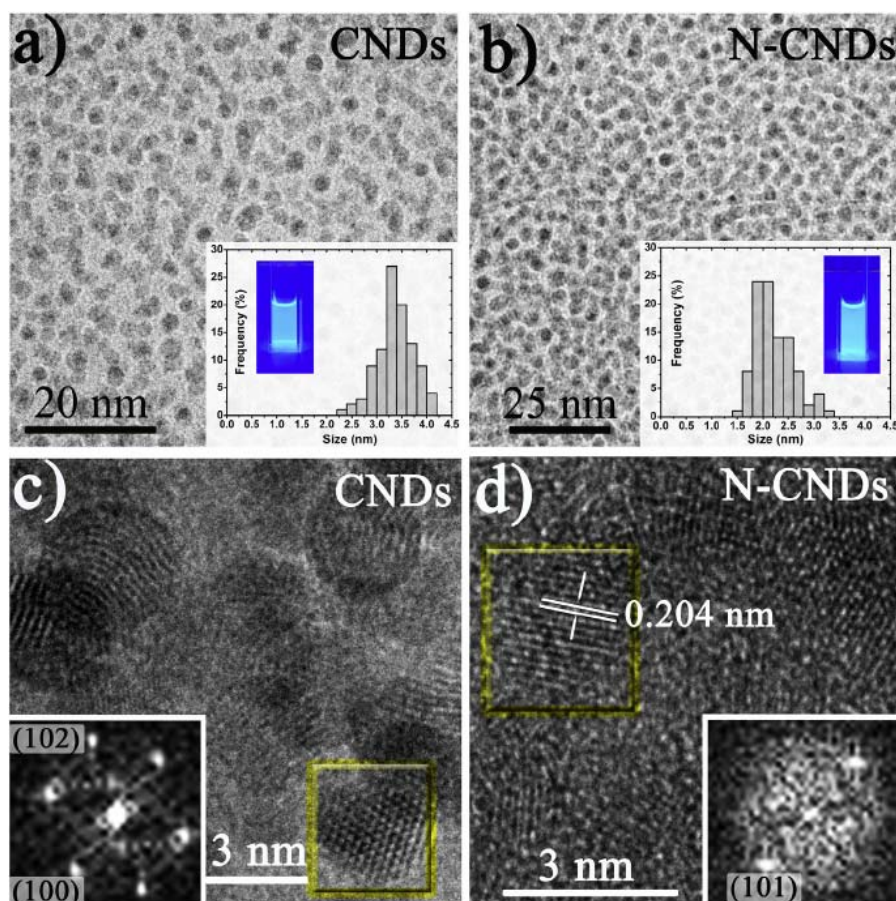
Fig. 3. Low magnification TEM images of the freestanding carbon nanodots after their release from the rod-shaped templates via ultrasonication and filtration: a) Undoped and b) N-doped CNDs, respectively. The insets in (a) and (b) reveal the particle size distribution determined for each type of CNDs and their emission under UV lamp illumination (365 nm); c-d) High resolution TEM images of the undoped and N-doped CNDs, respectively. The insets refer to the FFT analysis carried out on the nanoparticles highlighted in a yellow square and corresponding to graphitic diffraction spots. (A colour version of this figure can be viewed online.)

distribution of the CNDs estimated as 3.4 ± 0.4 nm and 2.3 ± 0.3 nm for the samples retrieved from CA and EDTA initial carbon precursors, respectively (Fig. 3). The differences observed for both carbon types in terms of average diameters are strongly dependent on the specific carbonization-passivation process for each organic precursor, as demonstrated in previous reports [28,29]. Average CNDs concentrations within the range of $1.00–1.25$ mg mL^{-1} were typically obtained with estimated 80% extraction efficiencies. No evidences of other organic aggregates could be detected by TEM inspection. Furthermore, the high pore diameter of the synthesized SBA-15 nanorods (8.43 nm determined by BET) has probably enabled a more straightforward release of the newly formed CNDs in contrast with former silica supports where chemical attacks and digestions were necessary to dissolve the inorganic templates and free the carbogenic cores [20,21]. The sample derived from CA will be hereafter labeled as undoped CNDs and the dots obtained from EDTA will be referred as N-doped CNDs.

The surface chemical composition of the CNDs was analyzed by X-ray photoelectron spectroscopy (XPS) resulting in 73.5% C and 26.5% O for the undoped CNDs and 71.5% C, 27.6% O and 0.9% N for the N-doped counterparts. Fig. 4 compares the high resolution C1s, O1s and N1s X-ray photoemission spectra corresponding to the undoped and the N-doped CNDs, respectively. Using curve-fitting analysis, the C1s contribution of the undoped CNDs can be mainly assigned to C—C bonds at 284.2 eV (37% intensity contribution) and to C—O (hydroxyl, ether-like) groups at 285.5 eV (28%

contribution). An additional and minor contribution of more oxidized species (i.e. carbonyl and carboxylic) at 287 and 288.9 eV further confirms the high presence of surface oxidized moieties dominating the first layers of the undoped CNDs. On the contrary, the N-CND sample shows a much lower contribution of highly oxidized species and its second major contribution is broader and shifted to higher binding energies (BEs). This can be attributed to the presence of C—O—C, C—OH and/or C—N species [30]. The O1s spectra show two main contributions of C/O species. The first one located at ~532.8 eV is usually associated to oxygen atoms bonded to C through sp^2 orbitals (i.e. aromatic species, carboxylic species) while the second is centered at ~531.5 eV and it is tentatively assigned to oxygen bonded to carbon through aliphatic sp^3 orbitals [31,32]. The relative contribution of each peak further corroborates the major presence of sp^3 bond-type in the N-doped sample. Finally, the evaluation of the N1s region confirms the presence of N within the carbon nanostructure prepared from the EDTA source and the negligible presence of any type of species in the undoped CNDs generated from CA. The peak at 399.3 eV can be attributed to N intercalated in terminal or bridge positions of the carbon network according to the criteria of Pels and Sanchez-Lopez [33,34].

Raman spectroscopy can be also used as a tool for the surface characterization of partially ordered carbon materials with an estimated analysis depth of 100 nm. The first-order Raman spectra corresponding to both CND samples reveal a similar pattern with two relatively broad bands centered at ~1350 cm^{-1} and ~1580 cm^{-1}
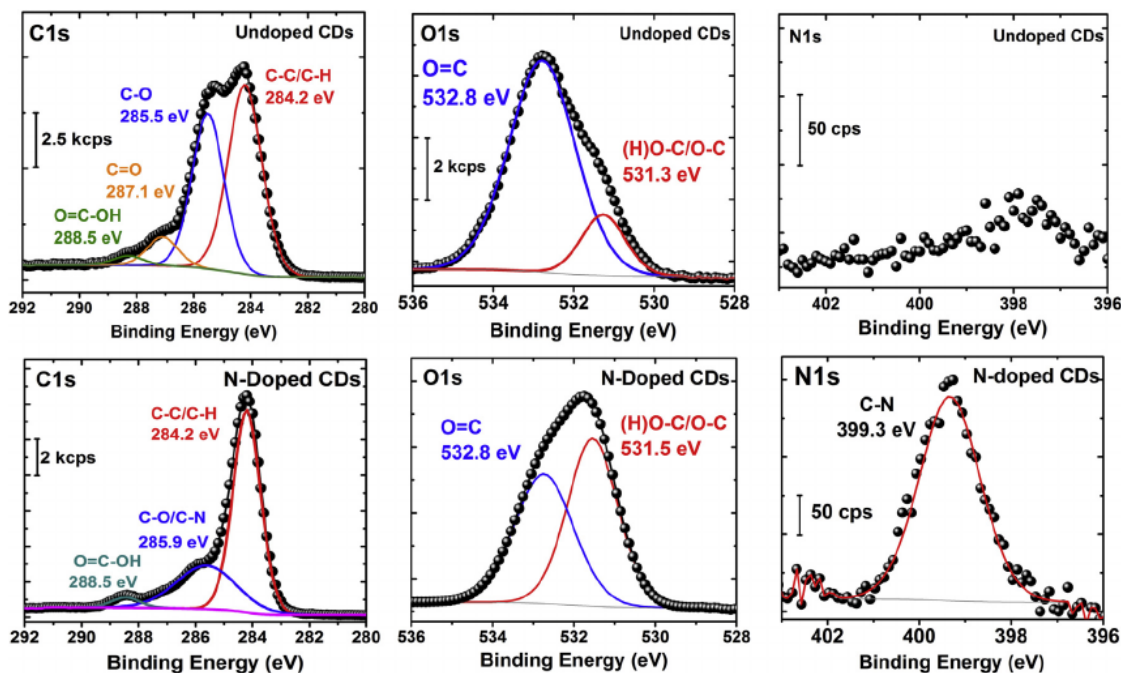
Fig. 4. Fitted X-ray photoelectron spectra (XPS) of the C1s, O1s and N1s regions corresponding to the undoped (upper row graphs) and N-doped CNDs (down row graphs). The result shows the atomic percentage of elements in each sample: O:C = 26.4:73.6 for the pure sample, and O:C:N = 27.6:71.5:0.9 for the N-doped one. (A colour version of this figure can be viewed online.)

with certain overlapping between them that are typically denoted as D band (typical of structural disorder and defects and sp^3 coordination) and G band (typical of graphitic order and sp^2 bonding), respectively (see Fig. S5). It is noteworthy that both samples seem to show a third contribution located at ~1505 cm^{-1} which has been previously denoted as D band and associated with amorphous sp^2-bonded forms of carbon interstitial defects, thereby pointing out to the existence of outer defective layers in CNDs [32]. The FTIR spectrum (Fig. S6) shows peaks around 3369 cm^{-1} corresponding to the stretching mode of the OH group. In undoped CNDs, the stretching vibrations of C=O and C—O at about 1634 and 1219 cm^{-1}, respectively, and the absorbance peak at 1053 cm^{-1} can be assigned to the epoxide group (C—O), thereby confirming the existence of oxidized species pointed out by XPS analysis. On the other hand, the N-doped CNDs exhibit peaks at 1627, 1387 and 1079 cm^{-1} belong to the stretching vibration, indicating that the existence of C=O, C—O—O$^-$ and C—O—C group, indicative to the presence of carboxylic group, and the stretch peak of C—C appears at 1347 cm^{-1}. The C—N stretch was also observed at 1310 cm^{-1} and the deformation vibration of —NH assigned at 1493 cm^{-1}, confirms the presence of N-doped species potentially attributable to amide, secondary amine or carbamate groups [30,33,34].

3.2. Optical characterization of colloidal undoped and N-doped CNDs

In Fig. 5 we present the optical characterization of the water-dispersed CNDs. Both undoped (Fig. 5a) and N-doped (Fig. 5c) CNDs show a strong optical absorption for UV excitations (<320 nm) with an absorption tail extending to the visible regime (absorption spectra depicted by the black dashed lines), as often observed for CNDs [1]. Typically, π-π^* (C=C), n-π^* (C=O) and σ-π^* transitions can be found around excitation wavelengths of 230—250, 300, and 330 nm, respectively [35,36]. While we could not separate the contributions of these transitions, a distinct band

appears at around 320 nm for the N-doped CNDs, which is attributed to the n-π^* transition induced by the amino groups at the surface [37]. The absorption enrichment due to the extra n-π^* transition is functional for photonic properties as it leads to emission enhancement (Fig. S7). Both colloidal systems show identical blue emission with the PL maximum around 420 nm. The origin of the emission of CNDs remains under debate, and could be the (combined) result of the following mechanisms: (i) the carbon core-related origin of emission resulting from the π-π^* transition of sp^2 clusters assisted by the QCE [1,38], (ii) the functional groups, surface states which behave as energy traps [39]. On one hand, we note that oxygen functional groups are generally considered to facilitate green-shifted emissions [40]. On the other hand, in first instance, the QCE model seems to be tackled by the size-independent emission as the undoped and N-doped CNDs have different average sizes. This can however be explained by the formation of several isolated sp^2 clusters within the carbon matrix which are responsible for the emission, with their size being independent of the total CND size. This is expected from the existence of both sp^2 and sp^3 bonded carbon (as observed by Raman spectroscopy in Fig. S5) and it is in line with other studies [36,41].

Furthermore, the PL tunability with excitation wavelength (visualized by the blue dashed lines in Fig. 5b and d) is generally found in carbon nanostructures [42,43]. It is attributed to multiple effects, such as the QCE,[33] surface traps,[39] or reorganization of the solvent's polarization [42—45], and is therefore still under debate [11]. According with our results, we tend to explain our excitation-dependence behavior from a simple down-shifting perspective; for broad emission spectra (whether originated from the QCE of size-dispersed sp^2 islands or simply because of surface traps), color tunability is inevitably achieved by down-conversion of excitations within the excitation spectrum. To our knowledge, all observations of excitation-dependent PL on CNDs are achieved by exciting the sample within the PL spectrum. This model, which we actually perceive as a PL shifting artifact, would explain most — if not all —
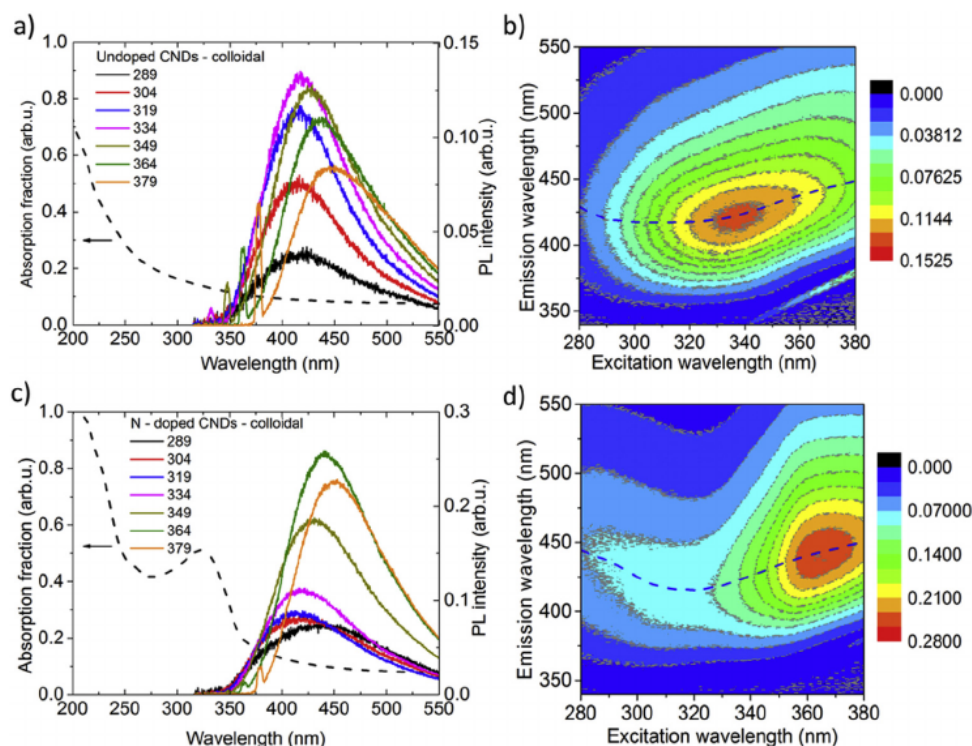
Fig. 5. Optical characterization of undoped (a, b) and N-doped (c, d) CNDs dispersed in water. (a, c) Absorption spectra (black dashed lines) combined with the PL spectra for a range of excitation wavelengths (289—379 nm) with steps of 15 nm, the sharp peaks correspond to the excitation wavelength. (b, d) Contour plot of several PLE spectra with the corresponding peak position of PL (blue dashed lines). (A colour version of this figure can be viewed online.)

interpretations of color tunability upon excitation [46—48]. This hypothesis is further strengthened by the fact that excitation-independent behavior is solely observed for excitations outside the PL spectrum [35,46].

3.3. Comparative optical behavior of colloidal and solid state CNDs

To exclude any potential interference of the solvent's polarity with the data presented in Fig. 5, we will further work with solid state samples. Upon drop casting the samples, the optical density decreases significantly but the feature of the n-π^* transition for the N-doped CNDs remains present (black dashed lines in Fig. 6a and c). The PL spectra of both samples, undoped and N-doped CNDs, now show a small red-shift (Fig. 6b and d). The emission at these longer wavelengths is typically related to the hybridized oxygen functional groups with the carbon core [49]. Hence, one possibility is that the oxidized surface states start dominating the emission process upon drop casting, as suggested before [46]. Another scenario that would red-shift the emission of the solid state sample is a change in the photonic mode density. Thirdly, energy transfer, either by re-absorption or by Förster resonant energy transfer (as often observed for semiconductor nanoparticles), could be another reason [50,51]. Since the drop casted CNDs are closely packed, both energy transfer processes would be seriously enhanced. Note that for systems that emit with efficiencies less than 100%, an enhancement of the energy transfer processes would result in a decrease of the PL quantum yield (PL QY); effect that will be addressed in the last part of the Results and Discussion section.

The so-called "giant red-edge effect" is used to explain the violation of Kasha's rule [52] which states that the fluorescence is independent on the excitation energy, by the reorganization of the solvent's polarity perpendicular to the dipole moment of the excited CNDs. We can test this model with our samples, since the

solid state and colloidal forms of the CNDs have similar emission spectra (only a small red-shift appears which might be the result, as we mention earlier, of energy transfer or changes in the functional groups emission). According to the "giant red-edge effect", the excitation-dependent behavior should be completely different (possibly even absent) for the solid state sample due to the absence of the polar solvent. However, both sample forms exhibit similar excitation-dependent PL spectra. This verifies that the excitation-dependent PL shift is not the result of the polarity of the solvent, but seems to result from down-shifting of excitations within the spectrum itself.

The time-resolved PL measurements of CNDs ($\lambda_{exc} = 360$ nm, $\lambda_{det} = 430$ nm) are shown in Fig. 7. Typically, single, double and triple exponential decay fitting curves are used to describe the behavior of CND PL lifetimes [39,49]. We clearly observe that the generated carriers decay through two mechanisms (see details in Supporting Information, Figs. S1 and S2). For short time-scales (up to several ns), the decay has a stretched exponential behavior, with the stretching coefficient β of around 0.7. The average lifetime of the stretched component (derived by making use of Guillois et al. [53]) varies from 0.55 to 0.95 ns depending on the sample state and the detection wavelength. At longer time-scales, the decay is single-exponential in nature, with a lifetime of around 5 ns for both solid state samples while it is a bit longer for colloidal samples, and it also increases as consequence of N-doping. The clear distinction of the two decay mechanisms implies that the generated carriers are separated into two different systems. The data can therefore not be explained by two decay paths that work on the same semi-stable state. Hence, a simple model of the competition of radiative and non-radiative recombination is not applicable. To our knowledge, the behavior for longer time-scales (being a single-exponential and the relation to the N-doping) suggests that it is originated from a molecular transition. Actually, single-exponential decay behaviors
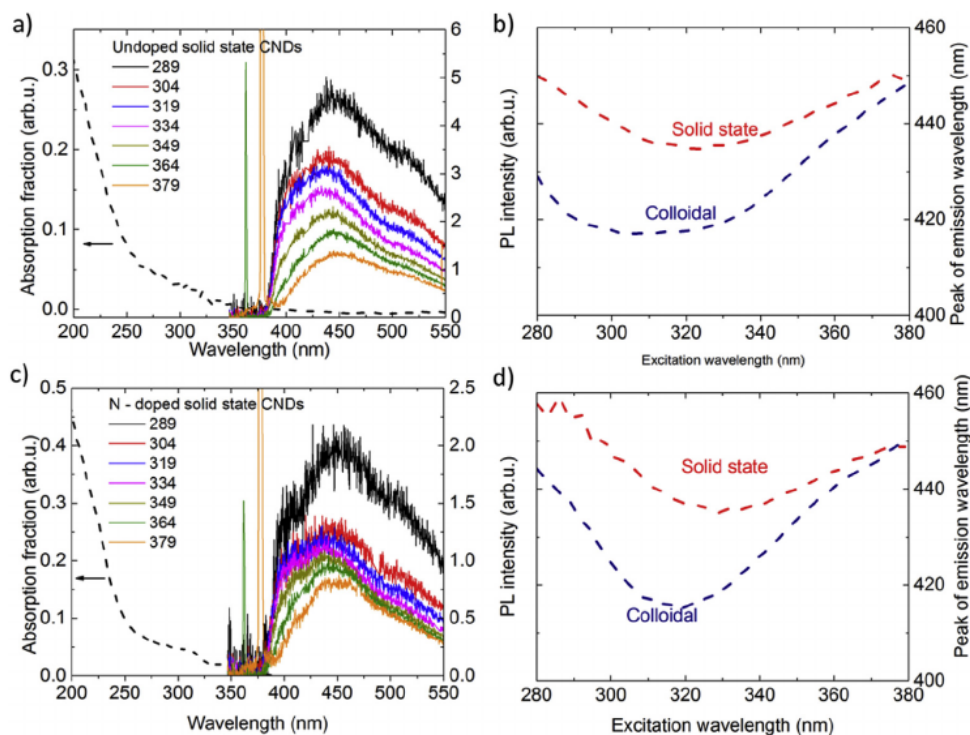
Fig. 6. Optical characterization of undoped (a, b) and N-doped (c, d) CNDs as solid state samples. (a, c) Absorption spectra (black dashed lines) combined with the PL spectra for a range of excitation wavelengths (280–380 nm, the excitation peaks which fall within the spectrum are shown) with steps of 15 nm. (b, d) Excitation dependence of the emission peak of the solid state (red) and the colloidal CNDs (blue). (A colour version of this figure can be viewed online.)
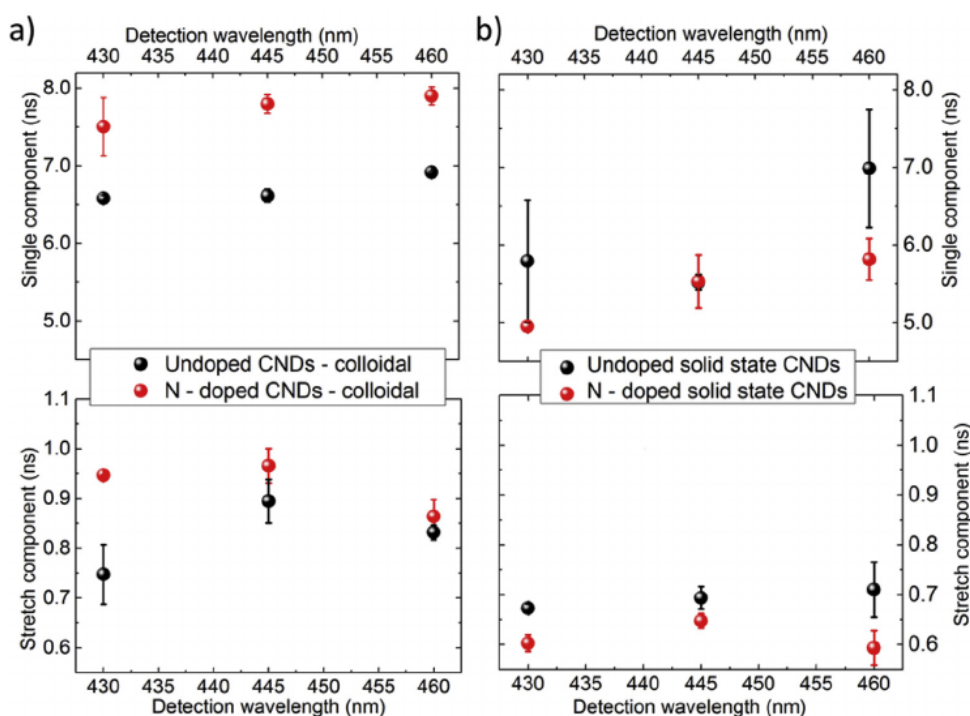

Fig. 7. Time-resolved PL measurements for undoped (black) and N-doped (red) CNDs. (a) Average lifetimes of the single (top) and stretched (bottom) components for water-dispersed CNDs as a function of detection wavelength. (b) Average lifetimes of the single (top) and stretched (bottom) components for the solid state samples as a function of detection wavelength. The depicted error describes the standard deviation of sequential measurements with different excitation powers in linear regime. (A colour version of this figure can be viewed online.)
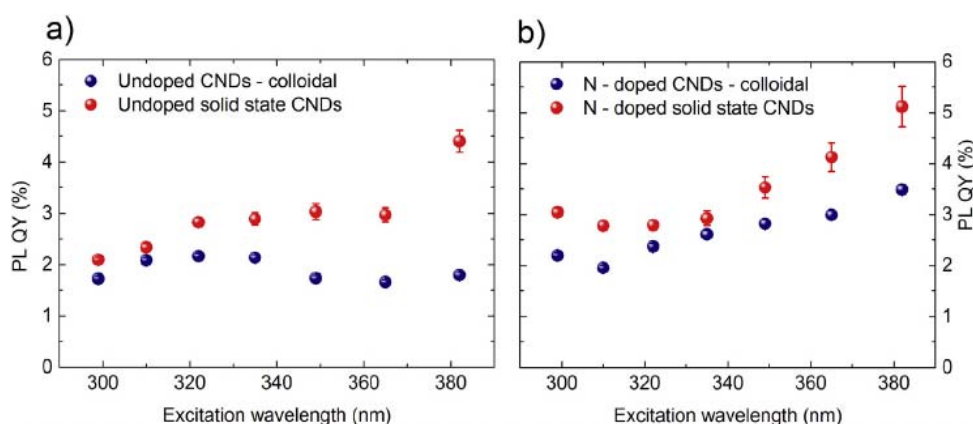
Fig. 8. PL QY of the undoped (a) and N-doped (b) CNDs, as a function of the excitation wavelength. The PL QY values of the colloidal CNDs are denoted in blue, whereas the red circles refer to the solid state CNDs. (A colour version of this figure can be viewed online.)

have been assigned to emission of C=O groups in COOH on N-doped CND surfaces, with lifetimes in the order of 15 ns, quite similar to our results [39].

In Fig. 8, we present the PL QY values as a function of the excitation wavelength, for the undoped and N-doped CNDs in colloidal and solid state. All samples show PL QY values in the range of 1–5%. Two main observations can be made: firstly, the N-doped CNDs (colloidal and solid state) have slightly higher emission efficiencies than their undoped counterparts; secondly, the emission efficiency increases upon drop casting. This latter observation rules out the energy transfer processes as mechanisms responsible for the spectral shifts observed in Fig. 6b and d since they would inevitably decrease the PL QY. We could explain this slight PL QY increase upon drop casting in line with Hao *et al.* [47], who stated that a transition of the PL mechanism arises due to more emission-efficient oxidized surface states. This also agrees with the slight red-shift observed in Fig. 6b and d. Regarding the first observation, it is well known that core emission can be improved by the incorporation of nitrogen [25,26]. Hence, the observed slight increase of the PL QY values of the N-doped CNDs suggests that the emission is still partly originated from the carbon core π-π^* transition of the sp^2 clusters (facilitated by the QCE).

4. Conclusions

The combination of a fluidized bed-assisted rapid pyrolysis with the confinement of precursors within an ordered nanoporous structure has been successfully validated as an efficient route to obtain highly uniform blue emissive undoped and N-doped CNDs with average sizes below 4 nm. This provided a uniform distribution of nanoparticles that allowed us to perform an in-depth study of their PL properties. The fluidized-bed assisted rapid pyrolysis represents a very convenient and appealing method given the short reactions required (below 6 min) and the highly reproducible reaction conditions afforded by the fluidizing environment. Furthermore, a thorough optical characterization of the generated CNDs both in colloidal and solid state has demonstrated that their emission (with an efficiency of 1–5%) originates from a combination of the QCE and the oxidized surface states. In addition, N-doping introduces resonant absorption states which participate in emission. By studying the behavior of different CNDs sample forms, colloidal and solid state, we have been able to explain the excitation-dependent/-independent mechanism with a simple model based on down-converting excitations in a broad emission spectrum, also valid for other CNDs reported in the literature.

Appendix A. Supplementary data

Supplementary data related to this article can be found at http://dx.doi.org/10.1016/j.carbon.2017.03.017.

Competing financial interests

The authors declare no competing financial interests.

References

[1] S. Zhu, Y. Song, X. Zhao, J. Shao, J. Zhang, B. Yang, The photoluminescence mechanism in carbon dots (graphene quantum dots, carbon nanodots, and polymer dots): current state and future perspective, Nano Res. 8 (2015) 355–381.
[2] S. Hu, A. Trinchi, P. Atkin, I. Cole, Tunable photoluminescence across the entire visible spectrum from carbon dots excited by white light, Angew. Chem. Int. Ed. 54 (2015) 2970–2974.
[3] H. Ding, S.-B. Yu, J.-S. Wei, H.-M. Xiong, Full-color light-emitting carbon dots with a surface-state-controlled luminescence mechanism, ACS Nano 10 (2016) 484–491.
[4] L. Himaja, P.S. Karthik, S.P. Singh, Carbon dots: the newest member of the carbon nanomaterials family, Chem. Rec. 15 (2015) 595–615.
[5] P. Miao, K. Han, Y. Tang, B. Wang, T. Linc, W. Chenga, Recent advances in carbon nanodots: synthesis, properties and biomedical applications, Nanoscale 7 (2015) 1586–1595.

[6] M. Havrdova, K. Hola, J. Skopalik, K. Tomankova, M. Petr, K. Cepe, et al., Toxicity of carbon dots e Effect of surface functionalization on the cell viability, reactive oxygen species generation and cell cycle, Carbon 99 (2016) 238–248.

[7] C.M. Zhang, J. Lin, Defect-related luminescent materials: synthesis, emission properties and applications, Chem. Soc. Rev. 41 (2012) 7938–7961.

[8] S.Y. Lim, W. Shen, Z.Q. Gao, Carbon quantum dots and their applications, Chem. Soc. Rev. 44 (2015) 362–381.

[9] M.C. Ortega-Liebana, J.L. Hueso, A. Larrea, V. Sebastian, J. Santamaria, Feroxyhyte nanoflakes coupled to up-converting carbon nanodots: a highly active, magnetically recoverable, fenton-like photocatalyst in the visible-nir range, Chem. Commun. 51 (2015) 16625–16628.

[10] M.C. Ortega-Liebana, J.L. Hueso, S. Ferdousi, K.L. Yeung, J. Santamaria, Nitrogen-doped luminescent carbon nanodots for optimal photo-generation of hydroxyl radicals and visible-light expanded photo-catalysis, Diam. Relat. Mater. 65 (2016) 176–182.

[11] Z. Gan, H. Xu, Y. Hao, Mechanism for excitation-dependent photoluminescence from graphene quantum dots and other graphene oxide derivates: consensus, debates and challenges, Nanoscale 8 (2016) 7794–7807.

[12] V. Nguyen, L. Yan, J. Si, X. Hou, Femtosecond laser-induced size reduction of carbon nanodots in solution: effect of laser fluence, spot size, and irradiation time, J. Appl. Phys. 117 (2015), 084304–1-084304-6.

[13] J. Deng, Q. Lu, N. Mi, H. Li, M. Liu, M. Xu, et al., Electrochemical synthesis of carbon nanodots directly from alcohols, Chem. Eur. J. 20 (2014) 4993–4999.

[14] J. Zhou, C. Booker, R. Li, X. Zhou, T.-G. Sham, X. Sun, Z. Ding, An Electrochemical avenue to blue luminescent nanocrystals from multiwalled carbon nanotubes (MWCNTs), J. Am. Chem. Soc. 129 (2007) 744–745.

[15] H. Li, X. He, Z. Kang, H. Huang, Y. Liu, J. Liu, S. Lian, C.H.A. Tsang, X. Yang, S.-T. Lee, Water-soluble fluorescent carbon quantum dots and photocatalyst design, Angew. Chem. 122 (2010) 4532–4536.

[16] M. Favaro, S. Agnoli, M. Cattelan, A. Moretto, C. Durante, S. Leonardi, J. Kunze-Liebhauser, O. Schneider, A. Gennaro, G. Granozzi, Shaping graphene oxide by electrochemistry: from foams to self-assembled molecular materials, Carbon 77 (2014) 405–415.

[17] Y. Liu, N. Xiao, N. Gong, H. Wang, X. Shi, W. Gu, L. Ye, One-step microwave-assisted polyol synthesis of green luminescent carbon dots as optical nanoprobes, Carbon 68 (2014) 259–264.

[18] Z. Wang, B. Fu, S. Zou, B. Duan, C. Chang, B. Yang, et al., Facile construction of carbon dots via acid catalytic hydrothermal method and their application for target imaging of cancer cells, Nano Res. 9 (2016) 214–223.

[19] J. Zhang, F. Abbasi, J. Claverie, An efficient templating approach for the synthesis of redispersible size-controllable carbon quantum dots from graphitic polymeric micelles, Chem. Eur. J. 21 (2015) 15142–15147.

[20] J. Zong, Y. Zhu, X. Yang, J. Shen, C. Li, Synthesis of photoluminescent carbogenic dots using mesoporous silica spheres as nanoreactors, Chem. Commun. 47 (2011) 764–766.

[21] H.G. Baldovi, S. Valencia, M. Alvaro, A.M. Asirib, H. Garcia, Highly fluorescent C-dots obtained by pyrolysis of quaternary ammonium ions trapped in all-silica ITQ-29 zeolite, Nanoscale 7 (2015) 1744–1752.

[22] C.E. Machado, L. Gazola Tartuci, H. de Fatima Gorgulho, L.F. Cappa de Oliveira, J. Bettini, D. Pereira dos Santos, et al., Influence of inert and oxidizing atmospheres on the physical and optical properties of luminescent carbon dots prepared through pyrolysis of a model molecule, Chem. Eur. J. 22 (2016) 4556–4563.

[23] R. Ramos, M.P. Pina, M. Menendez, J. Santamaria, G.S. Patience, Oxidative dehydrogenation of propane to propene: simulation of a commercial inert membrane reactor immersed in a fluidized bed, Can. J. Chem. Eng. 79 (2001) 902–912.

[24] J. Herguido, M. Menendez, J. Santamaria, On the use of fluidized bed catalytic reactors where reduction and oxidation zones are present simultaneously, Catal. Tod. 100 (2005) 181–189.

[25] H. Ding, J.-S. Wei, H.-M. Xiong, Nitrogen and sulfur co-doped carbon dots with strong blue luminescence, Nanoscale 6 (2014) 13817–13823.

[26] Y. Choi, B. Kang, J. Lee, S. Kim, G.T. Kim, H. Kang, et al., Integrative approach toward uncovering the origin of photoluminescence in dual heteroatom-doped carbon nanodots, Chem. Mater. 28 (2016) 6840–6847.

[27] E.M. Johansson, M.A. Ballem, J.M. Cordoba, M. Oden, Rapid synthesis of SBA-15 rods with variable lengths, widths, and tunable large pores, Langmuir 27 (2011) 4994–4999.

[28] Y.-P. Sun, B. Zhou, Y. Lin, W. Wang, K.A.S. Fernando, P. Pathak, M.J. Meziani, B.A. Harruff, X. Wang, H. Wang, P.G. Luo, H. Yang, M.E. Kose, B. Chen, L.M. Veca, S.-Y. Xie, Quantum-sized carbon dots for bright and colorful photoluminescence, J. Am. Chem. Soc. 128 (2006) 7756–7757.

[29] P.-C. Hsua, H.-T. Chang, Synthesis of high-quality carbon nanodots from hydrophilic compounds: role of functional groups, Chem. Commun. 48 (2012) 3984–3986.

[30] J.L. Hueso, J.P. Espinos, A. Caballero, J. Cotrino, A.R. Gonzalez-Elipe, XPS investigation of the reaction of carbon with NO, O$_2$, N$_2$ and H$_2$O plasmas, Carbon 45 (2007) 89–96.

[31] J.P. Boudou, A. Martinez-Alonzo, J.M.D. Tascon, Introduction of acidic groups at the surface of activated carbon by microwave-induced oxygen plasma at low pressure, Carbon 38 (2000) 1021–1029.

[32] J.P. Boudou, A. Martinez-Alonzo, J.M.D. Tascon, Oxygen plasma modification of pitch-based isotropic carbon fibres, Carbon 41 (2003) 41–56.

[33] J.R. Pels, F. Kapteijn, J.A. Moulijn, Q. Zhu, K.M. Thomas, Evolution of nitrogen functionalities in carbonaceous materials during pyrolysis, Carbon 33 (1995) 1641–1653.

[34] J.C. Sanchez-Lopez, C. Donnet, F. Lefebvre, C. Fernandez-Ramos, A. Fernandez, Bonding structure in amorphous carbon nitride: a spectroscopic and nuclear magnetic resonance study, J. Appl. Phys. 90 (2001) 675–681.

[35] Z.X. Gan, S.J. Xiong, X.L. Wu, T. Xu, X.B. Zhu, X. Gan, et al., Mechanism of photoluminescence from chemically derived graphene oxide: role of chemical reduction, Adv. Opt. Mater. 1 (2013) 926–932.

[36] Y. Wang, S. Kalytchuk, Y. Zhang, H. Shi, S.V. Kershaw, A.L. Rogach, Thickness-dependent full-color emission tunability in a flexible carbon dot ionogel, J. Phys. Chem. Lett. 5 (2014) 1412–1420.

[37] Y. Dong, H. Pang, H.B. Yang, C. Guo, J. Shao, Y. Chi, et al., Carbon-based dots co-doped with nitrogen and sulfur for high quantum yield and excitation-independent emission, Angew. Chem. Int. Ed. 52 (2013) 7800–7804.

[38] M.A. Sk, A. Ananthanarayanan, L. Huang, K.H. Lim, P. Chen, Revealing the tunable photoluminescence properties of graphene quantum dots, J. Mater. Chem. C 2 (2014) 6954–6960.

[39] H. Ding, H.-M. Xiong, Exploring the blue luminescence origin of nitrogen-doped carbon dots by controlling the water amount in synthesis, RSC Adv. 5 (2015) 66528–66533.

[40] H. Nie, M. Li, Q. Li, S. Liang, Y. Tan, L. Sheng, et al., Carbon dots with continuously tunable full-color emission and their application in ratiometric pH sensing, Chem. Mater. 26 (2014) 3104–3112.

[41] J.R. Rani, J. Lim, J. Oh, J.-W. Kim, H.S. Shin, J.H. Kim, et al., Epoxy to carbonyl group conversion in graphene oxide thin films: effect on structural and luminescent characteristics, J. Phys. Chem. C 116 (2012) 19010–19017.

[42] S. Khan, A. Gupta, N.C. Verma, C.K. Nandi, Time-resolved emission reveals ensemble of emissive states as the origin of multicolor fluorescence in carbon dots, Nano Lett. 15 (2015) 8300–8305.

[43] Y. Deng, X. Chen, F. Wang, X. Zhang, D. Zhao, D. Shen, Environment-dependent photon emission from solid state carbon dots and its mechanism, Nanoscale 6 (2014) 10388–10393.

[44] L. Cao, M.J. Meziani, S. Sahu, Y.P. Sun, Photoluminescence properties of graphene versus other carbon nanomaterials, Acc. Chem. Res. 46 (2013) 171–180.

[45] S.K. Cushing, M. Li, F. Huang, N. Wu, Origin of strong excitation wavelength dependent fluorescence of graphene oxide, ACS Nano 8 (2014) 1002–1013.

[46] S.J. Zhu, Q.N. Meng, L. Wang, J.H. Zhang, Y.B. Song, H. Jin, et al., Highly photoluminescent carbon dots for multicolor patterning, sensors, and bioimaging, Angew. Chem. Int. Ed. 52 (2013) 3953–3957.

[47] Y. Hao, Z. Gan, J. Xu, X. Wu, P.K. Chu, Poly(ethylene glycol)/carbon quantum dot composite solid films exhibiting intense and tunable blue-red emission, Appl. Surf. Sci. 311 (2014) 490–497.

[48] L. Pan, S. Sun, A. Zhang, K. Jiang, L. Zhang, C. Dong, et al., Truly Fluorescent excitation-dependent carbon dots and their applications in multicolor cellular imaging and multidimensional sensing, Adv. Mater. 27 (2015) 7782–7787.

[49] S.H. Jin, D.H. Kim, G.H. Jun, S.H. Hong, S. Jeon, Tuning the photoluminescence of graphene quantum dots through the charge transfer effect of functional groups, ACS Nano 7 (2013) 1239–1245.

[50] R. Limpens, A. Lesage, P. Stallinga, A.N. Poddubny, M. Fujii, T. Gregorkiewicz, Resonant energy transfer in Si nanocrystal solids, J. Phys. Chem. C 119 (2015) 19565–19570.

[51] C. De Weerd, L. Gomez, H. Zhang, W.J. Buma, G. Nedelcu, M.V. Kovalenko, T. Gregorkiewicz, Energy transfer between inorganic perovskite nanocrystals, J. Phys. Chem. C 120 (2016) 13310–13315.

[52] M. Kasha, Characterization of electronic transitions in complex molecules, Discuss. Faraday Soc. 9 (1950) 14–19.

[53] O. Guillos, N. Herlin-Boime, C. Reynaud, G. Ledoux, F. Huisken, Photoluminescence decay dynamics of noninteracting silicon nanocrystals, J. Appl. Phys. 95 (2004) 3677–3682.